Check for updates

The seismicity of Mars

D. Giardini [1]✉, P. Lognonné [2,3], W. B. Banerdt [4], W. T. Pike[5], U. Christensen[6], S. Ceylan [1], J. F. Clinton [7], M. van Driel[1], S. C. Stähler [1], M. Böse[1,7], R. F. Garcia[8], A. Khan[1,9], M. Panning[4], C. Perrin [2], D. Banfield[10], E. Beucler[11], C. Charalambous [5], F. Euchner [1], A. Horleston [12], A. Jacob[2], T. Kawamura[2], S. Kedar[4], G. Mainsant[8], J.-R. Scholz [6], S. E. Smrekar[4], A. Spiga [3,13], C. Agard[14], D. Antonangeli[15], S. Barkaoui[2], E. Barrett[4], P. Combes [14], V. Conejero[2], I. Daubar[16], M. Drilleau[2], C. Ferrier[14], T. Gabsi[2], T. Gudkova[17], K. Hurst[4], F. Karakostas[18], S. King [19], M. Knapmeyer [20], B. Knapmeyer-Endrun [21], R. Llorca-Cejudo[14], A. Lucas [2], L. Luno[14], L. Margerin[22], J. B. McClean[5], D. Mimoun [8], N. Murdoch[8], F. Nimmo [23], M. Nonon[14], C. Pardo [2], A. Rivoldini[24], J. A. Rodriguez Manfredi [25], H. Samuel[2], M. Schimmel [26], A. E. Stott[5], E. Stutzmann[2], N. Teanby [12], T. Warren[27], R. C. Weber[28], M. Wieczorek[29] and C. Yana [14]

The InSight (Interior Exploration using Seismic Investigations, Geodesy and Heat Transport) mission landed in Elysium Planitia on Mars on 26 November 2018 and fully deployed its seismometer by the end of February 2019. The mission aims to detect, characterize and locate seismic activity on Mars, and to further constrain the internal structure, composition and dynamics of the planet. Here, we present seismometer data recorded until 30 September 2019, which reveal that Mars is seismically active. We identify 174 marsquakes, comprising two distinct populations: 150 small-magnitude, high-frequency events with waves propagating at crustal depths and 24 low-frequency, subcrustal events of magnitude M_w 3–4 with waves propagating at various depths in the mantle. These marsquakes have spectral characteristics similar to the seismicity observed on the Earth and Moon. We determine that two of the largest detected marsquakes were located near the Cerberus Fossae fracture system. From the recorded seismicity, we constrain attenuation in the crust and mantle, and find indications of a potential low-S-wave-velocity layer in the upper mantle.

Sol 185 was a typical sol on Mars (a Mars sol is 24 h 39.5 min long, and we number sols starting from landing). The ground acceleration spectrogram recorded by the very broadband (VBB) instrument of SEIS[1–3] (Seismic Experiment for Interior Structure; Fig. 1a) is dominated by the noise produced by the weakly turbulent night-time winds and by the powerful, thermally driven convective turbulence during the day[4]. Around 17:00 local mean solar time (LMST), the wind fluctuations die out quite suddenly and the planet remains very quiet into the early night hours. Several distinctive features can be seen every sol on Mars. Lander vibrations activated by the wind appear as horizontal thin lines with frequency varying daily as a result of temperature variations of the

lander; almost invisible during quiet hours, they are not excited by seismic events (for example, the lander mode at 4 Hz in Fig. 1a). We also observe a pronounced ambient resonance at 2.4 Hz, strongest on the vertical component, with no clear link to wind strength but excited by all the seismic vibrations at that frequency. The relative excitations of the 2.4 Hz and 4 Hz modes serve as discriminants for the origin of ground vibrations recorded by SEIS, allowing us to distinguish between local vibrations induced by atmospheric or lander activity and more distant sources of ground vibrations. On Sol 185, two weak events can also be spotted in the quiet hours of the early evening, one with a broadband frequency content and a second 80 min later, centred on the 2.4 Hz resonance band (Fig. 1a).

¹Institute of Geophysics, Department of Earth Sciences, ETH Zurich, Zurich, Switzerland. ²Université de Paris, Institut de Physique du Globe de Paris, CNRS, Paris, France. ³Institut Universitaire de France, Paris, France. ⁴Jet Propulsion Laboratory, California Institute of Technology, Pasadena, CA, USA. ⁵Department of Electrical and Electronic Engineering, Imperial College London, London, UK. ⁶Max Planck Institute for Solar System Research, Göttingen, Germany. ⁷Swiss Seismological Service (SED), ETH Zurich, Zurich, Switzerland. ⁸Institut Supérieur de l'Aéronautique et de l'Espace SUPAERO, Toulouse, France. ⁹Institute of Theoretical Physics, University of Zurich, Zurich, Switzerland. ¹⁰Cornell Center for Astrophysics and Planetary Science, Cornell University, Ithaca, NY, USA. ¹¹Laboratoire de Planétologie et Géodynamique, Univ. Nantes, Univ. Angers, CNRS, Nantes, France. ¹²School of Earth Sciences, University of Bristol, Bristol, UK. ¹³Laboratoire de Météorologie Dynamique, Sorbonne University, Paris, France. ¹⁴Centre National d'Etudes Spatiales, Toulouse, France. ¹⁵Institut de Minéralogie, de Physique des Matériaux et de Cosmochimie, Muséum National d'Histoire Naturelle, Sorbonne University, Paris, France. ¹⁶Department of Earth, Environmental and Planetary Sciences, Brown University, Providence, RI, USA. ¹⁷Schmidt Institute of Physics of the Earth, Russian Academy of Sciences, Moscow, Russia. ¹⁸Department of Geology, University of Maryland, College Park, MD, USA. ¹⁹Department of Geosciences, Virginia Polytechnic Institute, Blacksburg, VA, USA. ²⁰DLR Institute of Planetary Research, Berlin, Germany. ²¹Bensberg Observatory, University of Cologne, Bergisch Gladbach, Germany. ²²Institut de Recherche en Astrophysique et Planétologie, Université Toulouse III Paul Sabatier, CNRS, CNES, Toulouse, France. ²³Dept. of Earth and Planetary Sciences, University of California Santa Cruz, Santa Cruz, CA, USA. ²⁴Royal Observatory of Belgium, Brussels, Belgium. ²⁵Centro de Astrobiología—Instituto Nacional de Tecnica Aeroespacial, Madrid, Spain. ²⁶The Institute of Earth Sciences Jaume Almera of the Spanish Scientific Research Council (ICTJA-CSIC), Barcelona, Spain. ²⁷University of Oxford, Department of Physics, Oxford, UK. ²⁸NASA Marshall Space Flight Center, Huntsville, AL, USA. ²⁹Université Côte d'Azur, Observatoire de la Côte d'Azur, CNRS, Laboratoire Lagrange, Nice, France. ✉e-mail: domenico.giardini@erdw.ethz.ch
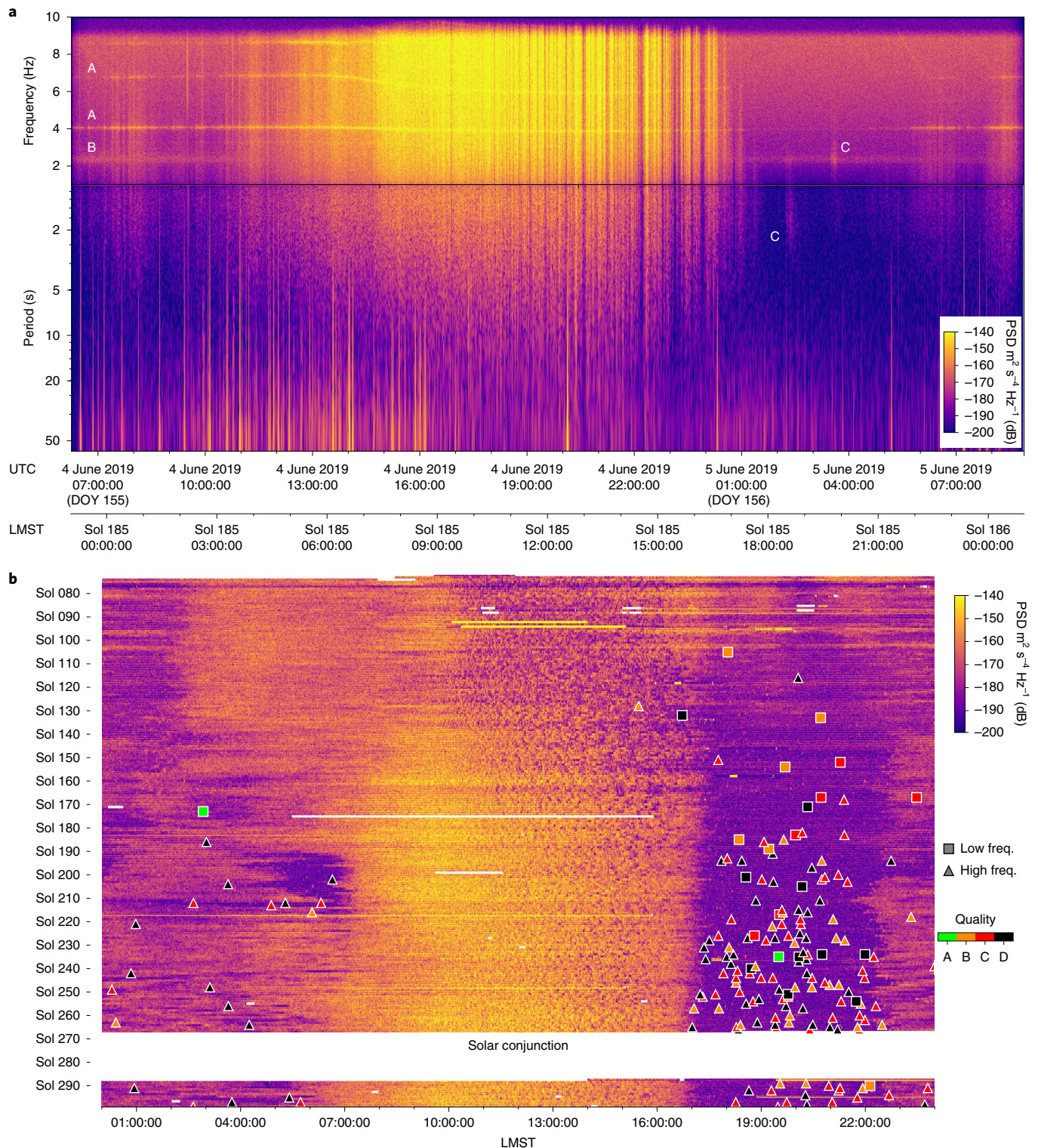
Fig. 1 | Spectrograms for Sol 185 and Sols 72–299. a, The spectrogram shows data in acceleration recorded at 20 samples per second for the vertical VBB component for Sol 185. We mark two modes excited by atmospheric perturbations and lander–ground coupling (A), the 2.4 Hz ambient resonance mode, which continuously exists throughout the day (B), and the two seismic events S0185a and S0185b, detected on Sol 185 (C). **b**, In the spectrogram stack, each horizontal line corresponds to a sol-long acceleration spectrogram from 20 s to 4 Hz for the vertical VBB component. White spaces indicate data gaps. The 174 detected events are marked with symbols corresponding to the event type, while event quality is indicated with colour. UTC, Coordinated Universal Time; DOY, day of year.

In the combined image for Sols 72 to 299 (Fig. 1b), the characteristic pattern of the wind noise and the events detected in the quiet evening hours can be tracked until 30 September (data were lost during 20 sols of solar conjunction). The Marsquake Service (MQS; see Methods for all details and procedures) detected 174 events, classified into two main categories: (1) low-frequency (LF) events with

energy content generally below 1 Hz, including some events with a more broadband content extending up to the 2.4 Hz resonance; (2) high-frequency (HF) events with energy above 1 Hz, reaching up to 6–12 Hz (smaller HF events can be seen only as narrowband excitation of the 2.4 Hz ambient resonance). The 174 events detected until Sol 299 include 24 LF and 150 HF events, of which 131 are visible only as 2.4 Hz resonance events. Most events were detected during very quiet hours that were devoid of recorded wind perturbations (Fig. 1b, see Methods and Supplementary Section 1) and have small signal amplitudes with accelerations as low as 10^{-10} m s^{-2}. A distinct characteristic is the visible increase over this period in the rate of HF events, whereas LF events appear to take place at a more uniform rate. The full Mars seismic catalogue and waveform data are available from ref. [5] and ref. [6], respectively.

Once a suspected event is identified, the first critical step of the MQS processing is discrimination between seismic energy and local spacecraft-, instrument- or atmospheric-induced perturbations (see Methods and Extended Data Figs. 1 and 2). Once we exclude an atmospheric or lander origin, we process each seismic event to determine P- and S-wave arrival times, distance, azimuth and magnitude[7–9]. Owing to the generally low signal-to-noise ratio (SNR), most seismic waveforms do not exhibit clear phase arrivals in the time domain, and the use of spectrograms and spectral envelopes have been the preferred method of both detection and investigation of seismic signals (Figs. 1a and 2).

The LF events display common characteristics. The signals have an overall duration of 10–20 min and most events show two distinct phases. Unambiguous P and S-phase identification based on polarization was possible only for the S0173a and S0235b events (Extended Data Fig. 3) and for the P phase for S0183a, as scattering prevents either positive or precise identification for all other events[2]. However, the similarity of the envelopes allows identification of the two phases as P and S for all events, in analogy to the waves observed for the larger events (Fig. 2). So far, we have not positively identified other phases such as depth phases (that is, pP, sP) or surface waves. No secondary P or S phases have been detected (for example, PP, SS, PcP, ScS) and we assume in this analysis that the observed P and S are the direct phases.

The HF events also display common features (Figs. 3b and 4b). The signal contains only HF energy with durations from 5 to 20 min, and most events show two separate peaks, interpreted as crustal P and S phases. A few events show only one dominant peak. The events observed as 2.4 Hz resonances have the same envelope shape as other HF events and we interpret them as low-amplitude HF events.

Extended Data Fig. 4 lists 13 LF and 23 HF events we use for further analysis in this paper. The SNR values of the selected LF events range from 2.5 to over 20, and peak-signal to peak-noise ratios range from 3.5 to over 200 (Extended Data Fig. 5). The LF and HF events define two separate families, with different origin, source depth and wave paths, providing first evidence on the seismic activity, seismic wave propagation and the internal structure of Mars.

Distance of LF events and constraints on mantle structure

The determination of epicentral distance using only one station and without sufficient knowledge of the internal velocity structure is challenging, especially with the lack of surface waves[10–12]. The MQS location procedure provides a probabilistic estimate of distance using an extensive a priori database of seismic velocity models to capture the epistemic uncertainty related to our lack of knowledge of the interior of Mars (Supplementary Section 2). The distance is then expressed as a probability density function (PDF) spanning the whole set of models and a source depth varying between 0 and 100 km.

Even at this early stage, we can check the compatibility of each model with the recorded data and eliminate many models. In

particular, over two-thirds of the a priori models predict an extensive S-wave shadow zone starting at around 20° distance and prove unable to match the S–P travel time differences measured for S0173a and S0235b; the allowed models tend to have a relatively thick crust (60–80 km) and a velocity increase or only a slight decrease below the Moho (Supplementary Section 2).

LF event alignment and indications of a low-velocity zone

Following in the tradition of classical seismology[13], we realign the events based on envelope similarity and using the travel time curves of the a priori V_P and V_S models of Mars. We display in Fig. 3a the preferred alignment with time and distance, with the caveat that the alignment process is not always unique in the case of low-amplitude events.

Families of events with similar characteristics are recognized:

1. Four events (S0235b, S0189a, S0105a, S0173a) with a dominant S-phase, good P and S arrival picks and a robust distance assessment are closely packed in distance between 25° and 29° (displayed in light orange colour in the lower panel of Fig. 3a; see also the enlargement in Extended Data Fig. 6). Two events (S0185a, S0234c) with larger S–P travel time are located in the distance range 58–64°. All six events show P and S phases with similar characteristics, indicating a common seismic origin at different distances.
2. Three events show a dominant P phase and only a small S-phase (dark grey). For S0183a, we identify the P phase based on polarization and a weak S-phase allows alignment of the event at ~46° distance. The shape of the P phase of S0205a indicates a very similar distance to S0183a. S0325a has mixed characteristics, with a similar P and a low-amplitude S, at a distance of ~35°. The similarity with the P phases of the other events in the panel located at closer and greater distances (Extended Data Fig. 6) points to a common seismic origin for all these events.
3. The upper panel in Fig. 3a displays four events (S0167a, S0154a, S0133a, S0226b; light red) for which we see no clear P phase or only a small emergent P phase, which are affected by large uncertainty. In addition, the S-phase-related wavepacket appears to be consistently longer than for the other events shown in the lower panel. For these reasons, we conclude that these events are located farther from the InSight station. The distance cannot be determined at this stage and we display the events aligned on a vertical line according to the S-phase picks, to illustrate the envelope similarity. The longer duration may be due to the presence of reflected phases or surface waves in the scattered tail of the S wave.

The sequence of events with similar P waves and dominant S waves around 25–30° and 58–64° epicentral distances, separated by events with only a small S wave at intermediate distance, provides the first evidence of a possible low-velocity zone for S waves on Mars, located in the 40–50° distance range (see also the detailed alignments of P and S phases in Extended Data Fig. 7). We explored alternative alignments, including the possibility that the decreasing S-wave amplitudes beyond 30° distance could be due to high attenuation in the deeper mantle below 300 km depth. This model, however, is inconsistent with the high-amplitude S waves observed at farther distances.

LF event spectra and anelastic mantle structure of Mars

The displacement spectra of earthquakes[14] and moonquakes[15,16] can be commonly approximated by a constant term proportional to the event's seismic moment, modulated by attenuation terms accounting for the source dimension and the anelastic attenuation: $A(f) = A_0 A_{src}(f) A_{att}(f)$. We also observe the same spectral shape for the LF events recorded on Mars (Fig. 4a), providing a validation that
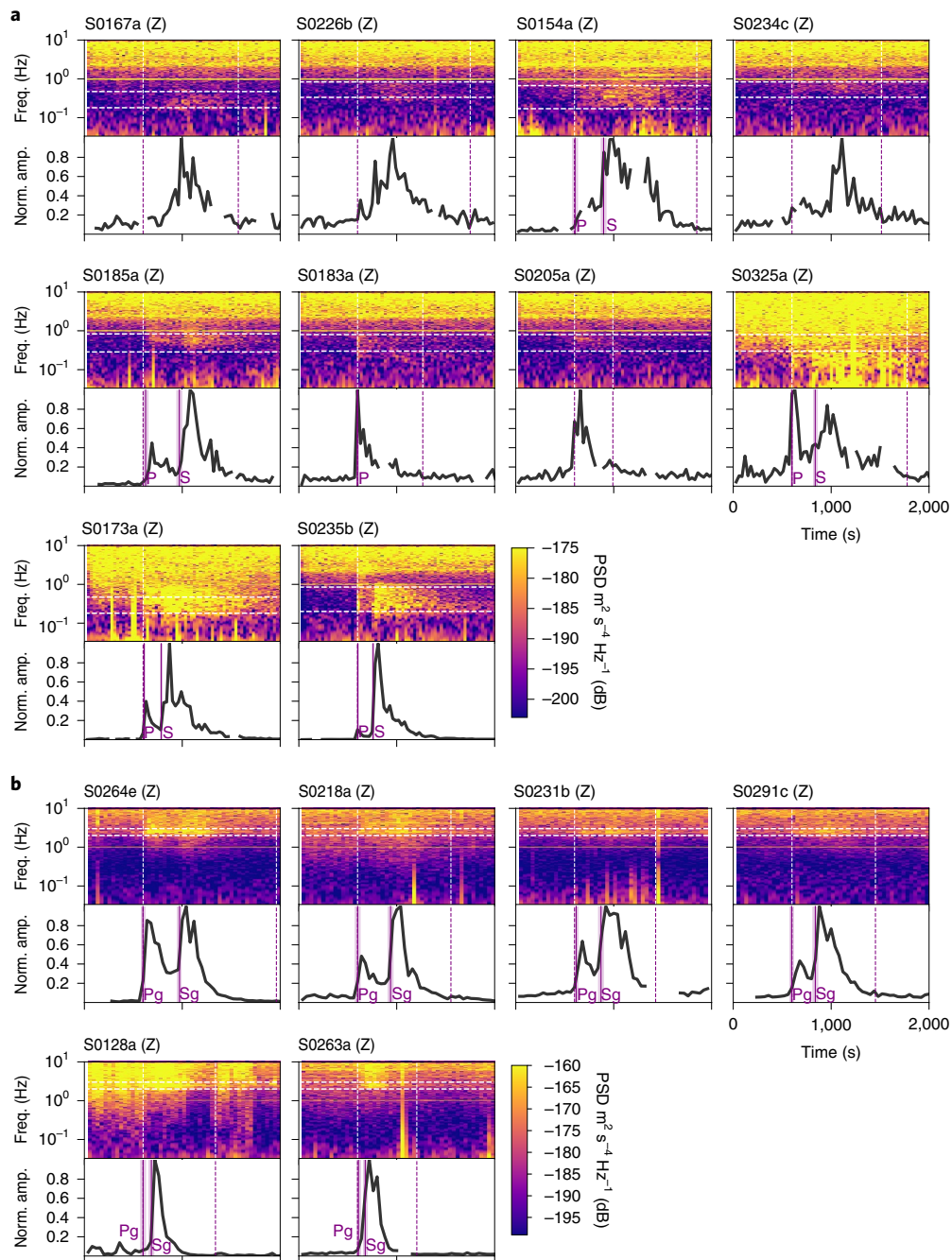
Fig. 2 | Spectral envelopes and acceleration power spectrograms. a, 10 LF events. **b**, 6 HF events. Vertical dashed lines indicate the signal start and end times selected by MQS for the events, while vertical solid lines show the picked P and S seismic phases, where available. The frequency band used for each event, shown with horizontal dashed lines, is manually picked to isolate the useful signal. Envelopes are computed by summing the spectral amplitudes over frequency. The spectrograms are calculated using window lengths of 60 s and 80 s for LF and HF events, respectively, with an overlap of 50%. Glitches are removed from the spectral envelopes for visual clarity.

the marsquake spectra obey similar scaling laws as quakes on the Earth and Moon.

Figure 4a compares modelled spectra (in blue) to the observed vertical and average horizontal spectra (in red) and with the noise spectra (in black). Using the magnitudes from the catalogue (see Methods) and the aligned distances (Fig. 3a), we achieve a consistent fit to the spectra, even for those events barely above noise level. The spectral fit provides an independent distance estimation for events for which the alignment could not be determined; this is

the case for S0167a, with a LF spectral content compatible with a distance of over 120°.

Because the LF events in our catalogue have small magnitudes, their corner frequencies, a measure of the duration and size of the event, are above 1 Hz. As a result, the decay of their spectra at high frequency is controlled by the attenuation term, and for each event we obtain an estimate of Q_{eff}, the effective attenuation parameter. Q_{eff} integrates contributions from scattering and intrinsic attenuation along the path and represents a lower bound on intrinsic Q.
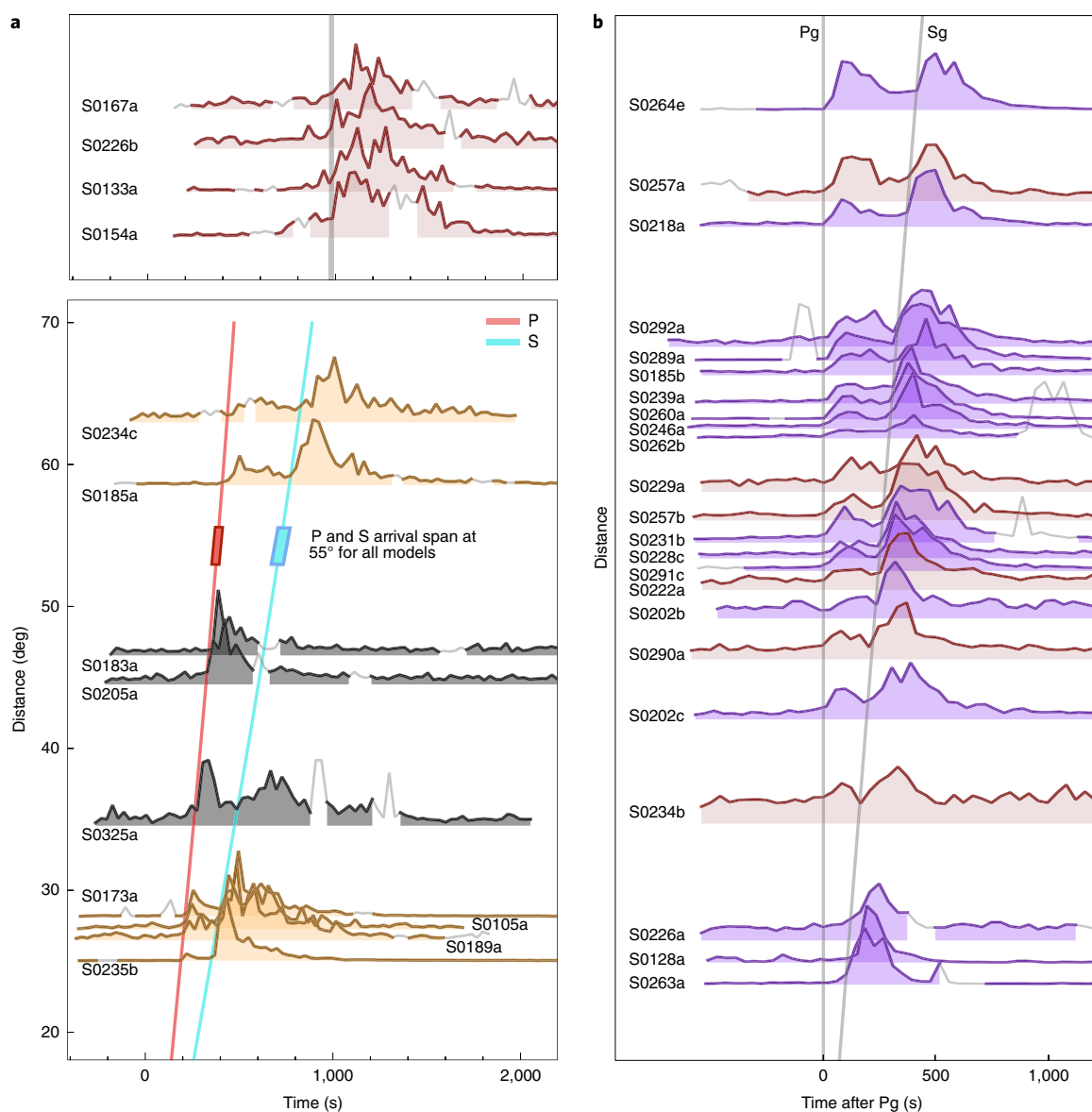
Fig. 3 | Event alignment with distance. Alignment is guided by spectral envelope similarity for LF events (**a**) and HF events (**b**), using the vertical component. Events in the bottom panel in **a** are aligned in distance by matching their P- and S-wave envelopes, with the exception of S0205a, where we observe only P phase. The vertical grey line in the top panel is used as reference to align the S-wave envelopes only. HF events in **b** are aligned using theoretical Pg and Sg group arrivals to show the relative distribution of these events in distance. Greyed-out portions of envelopes indicate glitches.

Because rays travel deeper with increasing epicentral distance, they sample material properties that are different from those seen by rays travelling in the lithosphere or upper layers of the mantle. The spectral fits of the events located at closer distance (Fig. 4a) are characterized by a Q_{eff} on the order of 300, while the spectra of more distant events require, instead, a Q_{eff} in excess of 1,000. This high value is consistent with the higher frequency content of these events, as illustrated by the broadband spectrum of S0185a, which reaches above 1 Hz and also shows a 2.4 Hz resonance amplification. The Q_{eff} observed for the more distant events is high in comparison to pre-mission shear attenuation (Q_μ) estimates of 75–350 for the deep mantle[17–21]. However, these values are derived from measurements of the tides raised on Mars by its closest moon Phobos, with a period of 5.55 h. The high value of the seismically observed Q_{eff} around periods of 1 s effectively constrains the visco-elastic behaviour of Mars and is of particular importance for understanding its thermal and rheological structure[18,22,23].

Figure 5 presents a schematic of the location of LF events below the Moho and the propagation of LF waves across the mantle and the low-velocity zone.

HF event alignment and crustal propagation
In Fig. 3b we align a selection of 23 HF events with distance using the separation of P and S phases. The HF content requires that these waves propagate in a low-attenuating medium, which appears to be different from the highly attenuating upper mantle traversed by the LF events at regional distance. We model the P and S wavepackets as multiply-reflected Pg and Sg energy trapped in the crust or in the upper layers of the crust. The trapped waves travel with crustal velocities and the distance spans a wide range, which is still uncertain and depends on the assumed velocity and depth of reflection. The P–S travel time difference for the farthest HF event, S0264e, would correspond to an epicentral distance ranging from almost 60° for a full crustal propagation with $V_S = 4\,km\,s^{-1}$ to 10–15° for a propagation

Fig. 4 | Displacement spectra. The spectra for the 10 LF events (**a**) and 6 HF events (**b**) in Fig. 2 (red) are compared to pre-event noise (black). The spectra are computed using a Brune source formulation for a stress drop of 1 MPa with an attenuation term using an effective quality factor Q_{eff} and a representative distance (blue dashed lines). For the HF events, the green dashed lines show a predicted spectrum purely from attenuation, with a flat source spectrum. The spectra are displayed for the vertical and average horizontal components. Time windows used for computation of the spectra are provided in Supplementary Table 3.1.

in slow shallow layers with $V_S = 700$–$1{,}000\,\mathrm{m\,s^{-1}}$. The distance and corresponding magnitude listed in Extended Data Fig. 4 are derived for an intermediate reference value of $V_S = 2.3\,\mathrm{km\,s^{-1}}$ and $V_P = 1.73 V_S$.

The observation of trapped waves is directly linked to event depth, as they can only be excited by events within the shallow crustal layers. This points to event depths in the crust for the HF events and below the Moho for the LF events. A mantle source for the LF events is also compatible with the absence of clearly developed surface waves.

The spectral plateau in Fig. 4b show that the HF events are consistently smaller than the recorded LF events, and because of this any LF content would be masked by noise. The corner frequency is typically around 6 Hz, though for some events is as high as 10–12 Hz. The possible contribution of the source duration is significant for these magnitudes at high frequency; however, a lower bound on attenuation on the propagation path in the crust or shallow layers can be derived by comparing model spectra incorporating both source and attenuation (blue lines, Fig. 4b) or only the attenuation decay (green lines) to the observed spectra (red lines). The high Q_{eff} values are compatible with the minimum intrinsic Q_i values derived

in ref. [2] for the shallowest layers of Mars. In the schematic in Fig. 5, the location of HF events in the crust and the propagation of multiply-reflected Pg and Sg phases is compared with LF events.

Among the most surprising characteristics of the HF events is the non-stationarity of their occurrence. We have carefully evaluated the evolution of the ambient noise and of the detection capacity of SEIS since deployment and can rule out that the increase in HF events occurrence is an artefact. We are evaluating possible causative models to explain a time-dependent, possibly seasonal, release of these quakes, related for example to orbital or thermal effects. Some of these models would indicate a very shallow origin of these events, which in turn could also indicate a closer epicentral distance.

Geographical distribution of seismicity on Mars

We can use the locations of the LF events to explore the geographical distribution of the observed seismicity, taking into account that we have retrieved complete locations only for three events so far, and that for the other events only the distance could be assessed.

In Fig. 6 we locate events on a map of the planet. Events S0235b, S0173a and S0183a are shown with their PDF solution in distance and azimuth (see inset), while for the other events we identify four

Fig. 5 | Schematic of wave propagation for the different event types. HF events excite trapped waves in the crust, while mantle waves are attenuated below the noise level. LF events are stronger, cannot excite trapped waves as they are located below the Moho, and the mantle waves are observed at long periods due to attenuation. A potential low-velocity layer (LVL) may explain the observed distance variation of S-wave amplitudes.
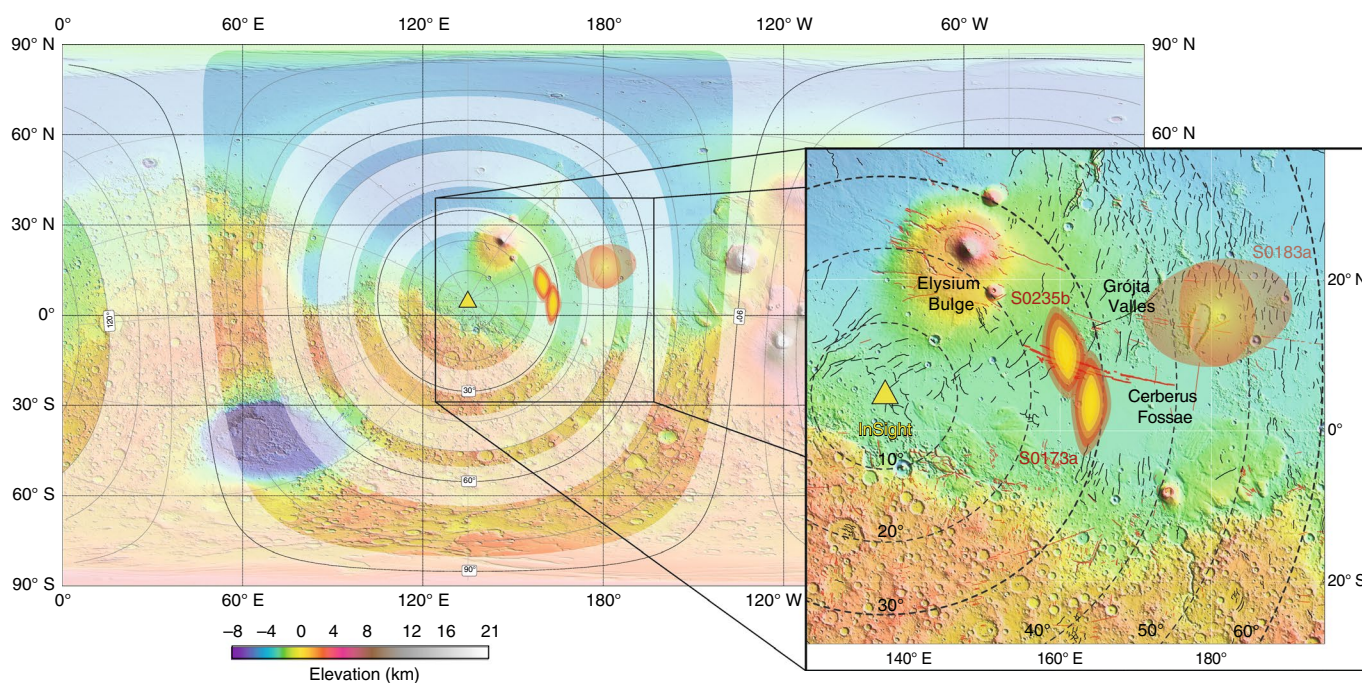
Fig. 6 | Global seismicity map of Mars shown on a Mars Orbiter Laser Altimeter (MOLA) elevation map. White shaded bands show the range of epicentral distances. Red to yellow ellipsoids are the estimated locations of events S0173a and S0235b; the estimated location of S0183a is displayed with two shaded ellipses, representing distance uncertainties of 5° and 10°. The inset to the right shows a map view of the epicentral area of the three event locations relative to the InSight landing site (yellow triangle), and associated with main surface fault traces for Cerberus Fossae, where black and red lines are main reverse and normal mapped faults, respectively (modified from ref. [30]).

circular zones drawn around the InSight location, following the distance alignment obtained in Fig. 3a. This unconventional style of mapping is necessary until we can better constrain the azimuth of the events, but nevertheless makes it possible to compare the distance ranges with possible active tectonic systems.

In particular, the robust control on the locations of the S0173a and S0235b events allows us to identify possible sources for these two marsquakes. Several major volcanic and tectonic structures are located near the InSight landing site (Supplementary Section 4). The uncertainty bounds of both events include the Cerberus Fossae region (inset, Fig. 6). These fossae were associated with possible

recent volcanic activity[24] and have been previously identified as a large and potentially active extensive tectonic structure close to InSight[25], where relatively fresh boulder traces hint at constant seismic activity[26]. The possible association of S0173a and S0235b to the active system of the Cerberus Fossae provides a strong indication that tectonic stress localization, as well as thermo-elastic cooling, may play an important role in the genesis of seismicity on Mars.

A common pattern in Earth's seismicity is the occurrence of aftershocks with similar characteristics to the mainshock. The first aftershock tentatively identified by MQS is S0235c, a small-magnitude event following 35 min after the much larger S0235b

event, with similar spectral characteristics, further supporting the marsquake nature of the seismic events on Mars.

Over 44 years since the first attempt by the Viking missions[27], the InSight SEIS instrument has revealed that Mars is seismically active. In the first 207 sols of data continuously recorded on Mars we detected 174 events that cannot be explained by local atmospheric- or lander-induced vibrations; these are interpreted as marsquakes. We identify two families of marsquakes: (1) 24 events of magnitude $M_w = 3–4$, located below the crust and with waves travelling inside the mantle and (2) 150 events of smaller magnitude and of closer distance, with waves trapped in the crust.

It is possible that a different type of source might explain individual seismic events. Alternative mechanisms that are being explored include meteorite impacts[28], infrasonic waves trapped in near-surface waveguides[29], episodes of underground fluid migration and gravitational phenomena such as mass wasting along impact crater walls in the vicinity of the landing site.

The first seismic observations on Mars deliver key new knowledge on the internal structure, composition and dynamics of the red planet, opening a new era for planetary seismology.

Online content

Any methods, additional references, Nature Research reporting summaries, source data, extended data, supplementary information, acknowledgements, peer review information; details of author contributions and competing interests; and statements of data and code availability are available at https://doi.org/10.1038/s41561-020-0539-8.

References

1. Banerdt, W. B. et al. Initial results from the InSight mission on Mars. *Nat. Geosci.* https://doi.org/10.1038/s41561-020-0544-y (2020).
2. Lognonné, P. et al. Constraints on the shallow elastic and anelastic structure of Mars from InSight seismic data. *Nat. Geosci.* https://doi.org/10.1038/s41561-020-0536-y (2020).
3. Lognonné, P. et al. SEIS: InSight's seismic experiment for internal structure of Mars. *Space Sci. Rev.* **215**, 12 (2019).
4. Banfield, D. et al. The atmosphere of Mars as observed by InSight. *Nat. Geosci.* https://doi.org/10.1038/s41561-020-0534-0 (2020).
5. InSight Marsquake Service. *Mars Seismic Catalogue, InSight Mission V1 2/1/2020* (ETHZ, IPGP, JPL, ICL, ISAE-Supaero, MPS, Univ Bristol, 2020); https://doi.org/10.12686/a6
6. InSight Mars SEIS Data Service. *SEIS raw data, Insight Mission* (IPGP, JPL, CNES, ETHZ, ICL, MPS, ISAE-Supaero, LPG, MFSC, 2019); https://doi.org/10.18715/SEIS.INSIGHT.XB_2016
7. Böse, M. et al. Magnitude scales for marsquakes. *Bull. Seismol. Soc. Am.* **108**, 2764–2777 (2018).
8. Böse, M. et al. A probabilistic framework for single-station location of seismicity on Earth and Mars. *Phys. Earth Planet. Inter.* **262**, 48–65 (2017).
9. Clinton, J. et al. The Marsquake Service: securing daily analysis of SEIS data and building the Martian seismicity catalogue for InSight. *Space Sci. Rev.* **214**, 133 (2018).
10. Panning, M. P. et al. Verifying single-station seismic approaches using Earth-based data: preparation for data return from the InSight mission to Mars. *Icarus* **248**, 230–242 (2015).
11. Khan, A. et al. Single-station and single-event marsquake location and inversion for structure using synthetic Martian waveforms. *Phys. Earth Planet. Inter.* **258**, 28–42 (2016).
12. van Driel, M. et al. Preparing for InSight: evaluation of the blind test for Martian seismicity. *Seismol. Res. Lett* **90**, 1518–1534 (2019).
13. Jeffreys, H. & Bullen, K. E. *Seismological Tables* (Office of the British Association for the Advancement of Science, 1940).
14. Brune, J. N. Tectonic stress and the spectra of seismic shear waves from earthquakes. *J. Geophys. Res.* **75**, 4997–5009 (1970).
15. Kawamura, T., Lognonné, P., Nishikawa, Y. & Tanaka, S. Evaluation of deep moonquake source parameters: implication for fault characteristics and thermal state. *J. Geophys. Res. Planets* **122**, 1487–1504 (2017).
16. Oberst, J. Unusually high stress drops associated with shallow moonquakes. *J. Geophys. Res. Atmos.* **92**, 1397–1405 (1987).
17. Bills, B. G., Neumann, G. A., Smith, D. E. & Zuber, M. T. Improved estimate of tidal dissipation within Mars from MOLA observations of the shadow of Phobos. *J. Geophys. Res. E Planets* **110**, E07004 (2005).
18. Khan, A. et al. A geophysical perspective on the bulk composition of Mars. *J. Geophys. Res. Planets* **123**, 575–611 (2018).
19. Lognonné, P. & Mosser, B. Planetary seismology. *Surv. Geophys.* **14**, 239–302 (1993).
20. Smrekar, S. E. et al. Pre-mission insights on the interior of Mars. *Space Sci. Rev.* **215**, 3 (2019).
21. Zharkov, V. N. & Gudkova, T. V. Construction of Martian interior model. *Sol. Syst. Res.* **39**, 343–373 (2005).
22. Bagheri, A., Khan, A., Al-Attar, D., Crawford, O. & Giardini, D. Tidal response of Mars constrained from laboratory-based viscoelastic dissipation models and geophysical data. *J. Geophys. Res. Planets* **124**, 2703–2727 (2019).
23. Nimmo, F. & Faul, U. H. Dissipation at tidal and seismic frequencies in a melt-free, anhydrous Mars. *J. Geophys. Res. E Planets* **118**, 2558–2569 (2013).
24. Vaucher, J. et al. The morphologies of volcanic landforms at Central Elysium Planitia: evidence for recent and fluid lavas on Mars. *Icarus* **200**, 39–51 (2009).
25. Taylor, J., Teanby, N. A. & Wookey, J. Estimates of seismic activity in the Cerberus Fossae region of Mars. *J. Geophys. Res. E Planets* **118**, 2570–2581 (2013).
26. Brown, J. R. & Roberts, G. P. Possible evidence for variation in magnitude for marsquakes from fallen boulder populations, Grjota Valles, Mars. *J. Geophys. Res. Planets* **124**, 801–822 (2019).
27. Anderson, D. L. et al. Seismology on Mars. *J. Geophys. Res.* **82**, 4524–4546 (1977).
28. Daubar, I. et al. Impact-seismic investigations of the InSight mission. *Space Sci. Rev.* **214**, 132 (2018).
29. Garcia, R. F. et al. Finite-difference modeling of acoustic and gravity wave propagation in Mars atmosphere: application to infrasounds emitted by meteor impacts. *Space Sci. Rev.* **211**, 547–570 (2017).
30. Knapmeyer, M. et al. Working models for spatial distribution and level of Mars' seismicity. *J. Geophys. Res. E Planets* **111**, E11006 (2006).

Methods

MQS procedures for event detection, event characterization and catalogue management. SEIS data are retrieved by SISMOC (SEIS on Mars Operations Center) on Earth, prepared for analysis and automatically delivered to both the MSDS (Mars SEIS Data Service) for distribution to the InSight science team and to the MQS. The MQS is tasked with analysis of the SEIS dataset and curation of the marsquake catalogue, reacting every day as new data are downloaded from Mars[9]. MQS frontline seismologists on duty are charged with initial data screening and preliminary event characterization. The MQS review team routinely convenes to confirm the frontline analysis.

Seismic event detection and discrimination. Once the MQS frontline person on duty is informed that there are new data available, the search for marsquakes begins. Seismic events identified so far are characterized by energy between ~0.1 and 10 Hz, durations ranging from 5 to 30 min and typically have amplitudes only slightly above the lowest background noise, which occurs only for a few hours each sol. We automatically produce spectrograms for each sol and all channels, updated with each new data arrival. The seismologist on duty scans through time series and spectrograms looking for features within this energy band to identify any candidate seismic signals, and then works to ensure the signal cannot be explained by any non-seismic phenomena. Here, we take the example of Sol 189, during which a typical event occurs, to illustrate our detection and discrimination procedures.

1. Detection and first discrimination. The sol-long spectrogram from the VBB vertical component spectrogram is shown in the top part of Extended Data Fig. 1a. A candidate seismic band of energy is visible in the middle of the quietest period; the lower part of Extended Data Fig. 1a shows the spectrogram zoomed into this period, with event energy start and end times as identified by MQS. Extended Data Fig. 1b,c shows various waveforms from the same zoomed time period. Extended Data Fig. 1b presents the three components of VBB velocity seismograms filtered between 1.2 and 2.8 s. Extended Data Fig. 1c displays the auxiliary channels for pressure (detrended), wind direction and wind speed, as well as the three magnetic channels. In addition, MQS has access to known spacecraft activity, such as robotic arm movement and lander communication. These datasets are always checked to ensure there are no anomalous atmospheric or lander signals that correlate with seismic signals. In this case, there is lander communication activity (UHF radio transmission) that clearly affects the magnetic channels (grey shaded area, Extended Data Fig. 1c), but this concludes some minutes before the seismic energy starts. There is no indication of an anomalous signal in the pressure signal, and for the majority of the signal, the wind speed is at or below the sensitivity of the TWINS instrument (2.8 m s^{-1}). Furthermore, there is no visible wind excitation of lander modes.

2. Direct comparison of wind and seismic data. Because the amplitudes of the seismic signals are generally very small and only just above the background noise within a relatively narrow frequency band, wind contamination is of particular concern. Extended Data Fig. 2 shows seismic and wind signals from a wider time window for Sol 189 (indicated by the horizontal grey bar above the top spectrogram in Extended Data Fig. 1). Significant wind speed and direction changes occur during the turbulent period, hours before the seismic energy begins. However, during the quieter period when this event occurs, the wind recorded by TWINS is mostly between 1.8 and 2.8 m s^{-1}, with wind bursts up to 3.5 m s^{-1}.

Following this set of analyses, MQS concludes the signal cannot be explained by atmospheric or lander signals and is of seismic origin. Once an event is confirmed, it is added into our database and it is labelled following the convention S[xxxx][z]; where [xxxx] indicates the InSight mission sol on which the event begins (starting from Sol 0, the sol when InSight landed on Mars) and [z] is a letter that ensures unique names if multiple events occur on a single sol. This particular event is assigned the event name of S0189a.

In the period following this first detection, various efforts continue to be made to understand the possible effects of weather on the observed seismic signal and provide estimates of the strength of the seismic signal. These methods are described in detail in Supplementary Section 1, with application to the S0189a event.

Seismic event characterization. Once an event is considered to be seismic, we proceed to characterization, which is illustrated here using the LF event on Sol 235, S0235b, one of the largest events recorded so far. For all events, MQS will try to make a single station location for the event, which involves various stages:

1. Phase picking. We assign pick uncertainties that reflect the sharpness of observed energy onsets, guided both by the spectrogram and, if possible, also the filtered time series. Typically, for picks guided by the spectrogram, MQS selects uncertainties between ±10 and 60 s; for picks that are directly visible in the time series, picks are selected on a single component and uncertainties are between ±1 and 2 s. There are two picks made for S0235b, both with ±2 s uncertainty, as shown on the velocity time series in Extended Data Fig. 1. At this stage, the phase type is not known, and according to the naming convention of the International Association of Seismology and Physics of the Earth's Interior, the first onset energy phase is assigned to be x1, subsequent phases are x2 and so on. For HF events, slope breaks on an STA-LTA (Short Time Average over Long Time Average) filter centred on 2.4 Hz are used to identify phases.

2. Phase polarization. MQS also makes a polarization analysis for degree of ellipticity, azimuth and inclination. For the majority of phases, there is no obvious polarization. For the largest LF events, the polarization is clear for a few seconds following the arrivals, before breaking down. Extended Data Fig. 1 provides hodograms indicating the azimuth for each of the two identified arrivals for S0235b. For x1 on S0235b, the polarization is 74°, while x2 clearly has a different polarization angle.

3. Phase association. In general, it is challenging to assign phase types to the arrivals. In the absence of clear polarization, we infer and assign phases to x1 and x2: P- and S-wave arrivals for LF events; Pg and Sg for HF events. In the case of S0235b, the clear change in polarization provides an additional indication that we are looking at P and S arrivals. The selected back azimuth for this event is 74° from the P-wave train. So far, only first arriving P/Pg and S/Sg phases have been assigned to events.

4. Distance, back azimuth and location. Because S0235b has both P and S phases assigned, as well as a polarization of the P wave, following ref. [8] and Supplementary Section 2, we can calculate (1) a preferred absolute distance of 26° and (2) a back azimuth of 74°, and a location at 11° N, 161° E. For the majority of events, at most, the distance can be provided.

5. Event type and quality are assigned to all events. The event type reflects the frequency content as discussed in the main text (LF and HF). The event quality is assigned according to the following conventions:

    A. High-quality events: multiple clear and identifiable phases and clear polarization (that is, location available).
    B. Medium-quality events: multiple clear and identifiable phases but no polarization (distance available, but no azimuth and hence no unique location).
    C. Low-quality events: signal clearly observed but phase picking is challenging.
    D. Weak or suspicious events.

    S0235b is classified as an LF quality A event.

6. Magnitudes are assigned according to scales tailored for Mars[7] with an updated calibration reflecting the actual data and observed events (Supplementary Section 3). For each event several magnitudes are computed, depending on the availability of different phases. The LF events observed so far are all in the magnitude range M_w 3–4, while the more local HF events are in the range M_w 1–2.3 (accounting also for the large uncertainty in distance). S0235b has magnitude M_w 3.6.

Further event revision. All events are periodically revised according to the distance alignment procedure outlined in the main text. When phases are clear and impulsive, no changes or minimal realignments are made. For some events, major realignments are made, guided by waveform similarity, reassignment of initial phase association or indications that phases are emerging and pick times do not correctly reflect the phase onset.

Event catalogue. In the period up to Sol 299, over 174 events have been identified in the data. Extended Data Fig. 4 includes the key characteristics for the 36 LF and HF events, including S0189a and S0235b described above. We indicate pick times and uncertainties for P/Pg and S/Sg phases, and distances from both catalogue locations and realignment. The complete catalogue including all events is available at ref. [5].

Data availability

The InSight seismic event catalogue[5] and waveform data[6] are available from the IRIS-DMC and SEIS-InSight data portal (https://www.seis-insight.eu/en/science). The catalogue and waveform data have the identifiers https://doi.org/10.12686/a6 and https://doi.org/10.18715/SEIS.INSIGHT.XB_2016, respectively. Seismic waveforms as well as data from all other InSight instruments and MOLA topographic data are available from NASA PDS (https://pds.nasa.gov/).

Code availability

The analyses in this study were conducted using a suite of custom software tools. The source codes can be made available from the Marsquake Service upon request (savas.ceylan@erdw.ethz.ch).

Author contributions

D.G. coordinated the seismological interpretations and wrote the manuscript. P.L. led the SEIS experiment and the VBB sensor work, and designed the higher-level requirements of the experiment together with D.M. W.B.B. led the InSight mission and the US contribution to SEIS. D.G., P.L., W.T.P. and U.C. led SEIS subsystems work. S.C., J.F.C., M.v.D. and S.C.S. contributed figures and to the writing of the main text and methods. S.C., J.F.C., S.C.S., M.v.D., M.B., R.F.G., A.K., M.P., C. Perrin, P.L. and W.T.P. provided seismological analyses. J.F.C., M.B., S.C., C.C., M.v.D., A.H., A.K., T.K., G.M., J-R.S. and S.C.S. were the Marsquake Service frontline team leading first data analysis. D.G., W.B.B., D.B., R.F.G., S.K., P.L., M.P, W.T.P., S.E.S., A.S. and R.C.W., in addition to the frontline team members, served in the Marsquake Service review team. F.E. led the MQS operational software development, and E. Beucler, C. Perrin, S.C.S. and S.C. managed Event Request Proposals. A.S. and D.B. managed the Mars Weather Service. D.B. and J.A.R.M. led the InSight APSS and TWINS instruments. On-board flight software was coordinated by R.L.-C. and M.N. I.D., N.T. and F.K. led the investigation into impacts, and A.L. and S.K. contributed on other non-seismic sources. N.M., K.H., D.M. and B.K.-E. contributed to lander modes and noise. Additional seismological contributions were from L.M., E.S., M.D., M.S., S.B., T.W. and J.B.M. Martian velocity models and discussions were contributed by A.K., A.R., H.S., T. Gudkova, S.K., F.N. and D.A. MSDS services were operated by C. Pardo and V.C., while T. Gabsi led the VBB operations at IPGP and contributed to the tests and Mars commissioning. L.L., C.F., C.A. and P.C. performed SISMOC ground services. E. Barrett contributed to SEIS operations and C.Y. led SEIS operations. Methods were contributed by J.F.C., S.C., S.C.S., M.v.D., C.C., W.T.P. and P.L. Supplementary Section 1 was contributed by P.L., R.F.G., W.T.P., C.C., A.E.S., S.C. and S.C.S., Supplementary Section 2 by A.K., A.R. and H.S., Supplementary Section 3 by M.B. and S.C.S. and Supplementary Section 4 by C. Perrin, A.J. and M.K. All authors read and commented on the manuscript.

Competing interests

The authors declare no competing interests.

Additional information

Extended data is available for this paper at https://doi.org/10.1038/s41561-020-0539-8.

Supplementary information is available for this paper at https://doi.org/10.1038/s41561-020-0539-8.

**Correspondence and requests for materials** should be addressed to D.G.

Peer review information Primary Handling Editor: Stefan Lachowycz.

Reprints and permissions information is available at www.nature.com/reprints.
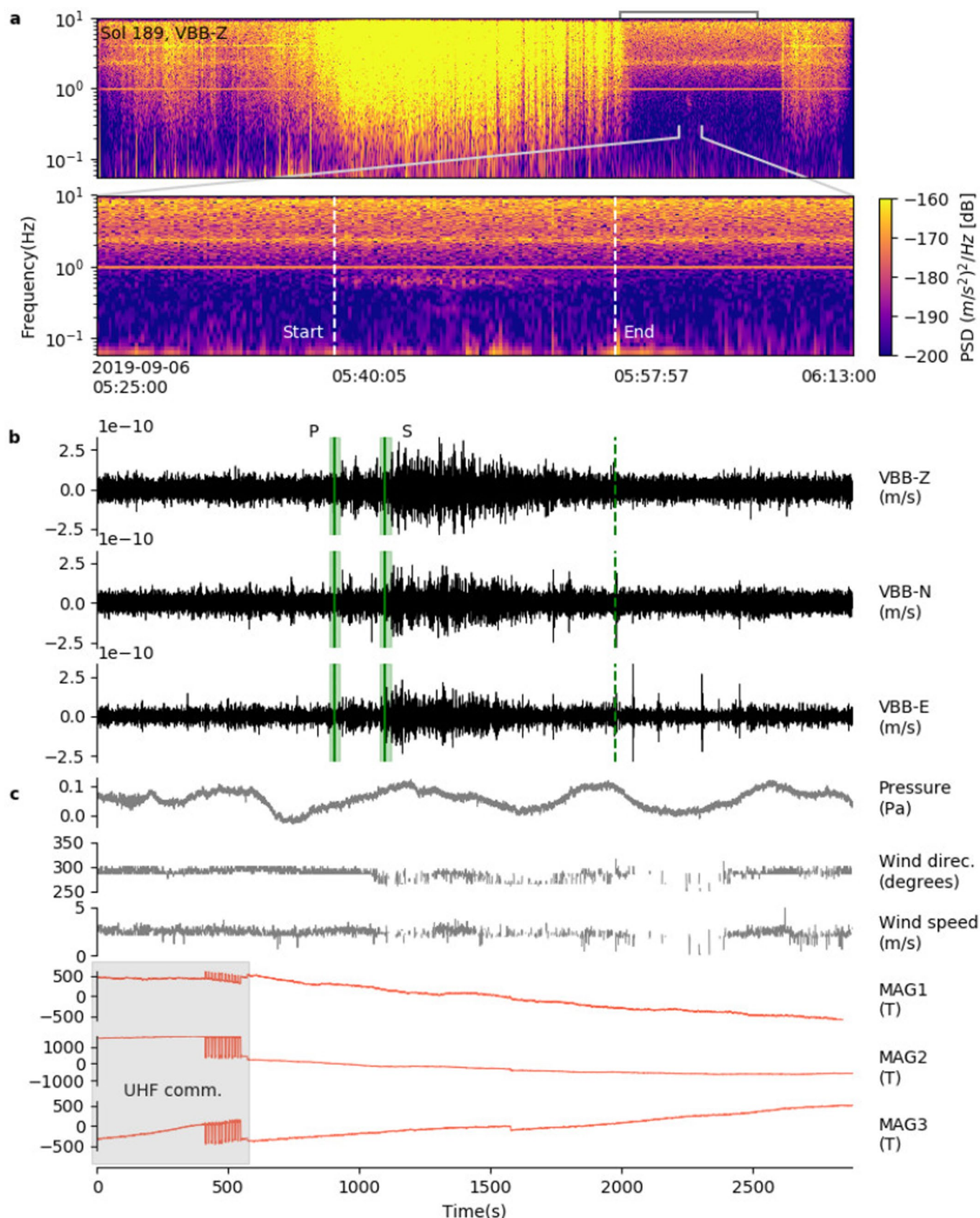
Extended Data Fig 1 | Analysis of the seismic event observed on Sol 189. a, Acceleration spectrogram for entire sol (top) and zoom around the event (bottom) with event start and end times (UTC) marked. **b**, Three component seismic channels in m/s (VBB, 20 sps) with MQS phase picks and uncertainties. **c**, Auxiliary channels used when analysing the data. Timing of **b** and **c** match the bottom spectrogram in **a**. VBB is the very broadband seismometer, and MAG1/2/3 are the three magnetometer channels. The only lander activity during the event period (UHF communication) is marked with shaded area on the MAG channels. Time span shown in Extended Data Fig. 2 is marked in the 24hour window at the top of **a**.
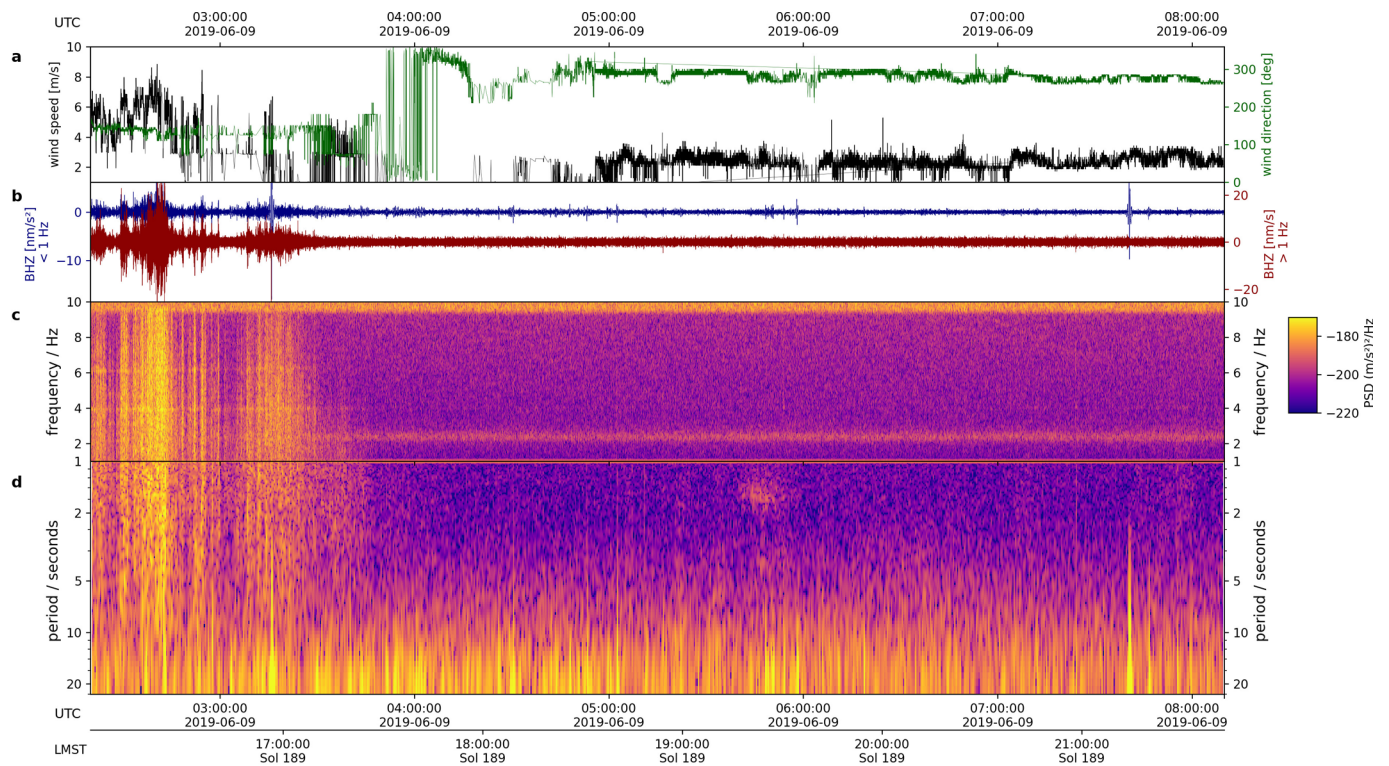
Extended Data Fig 2 | Comparison of wind and seismic data in a 5-hour period centred around the seismic event on Sol 189. a, Wind speed (black) and direction (green), **b**, vertical 20sps VBB data with 1s high pass (blue) and 1s low pass (red) filters, **c** and **d**, spectrogram of seismic channel. The wind speed is below 2.8 m/s for the majority of the seismic event, as it is for much of quiet evening period. While a wind direction change of 30 degrees was recorded during the event by the TWINS sensor, the longer context shows that this is occurring about once per hour and is likely an artefact of the sensor at very low wind speeds. As described in [4], the TWINS sensor does not report reliable wind speeds and directions below a wind speed of 2.8 m/s.
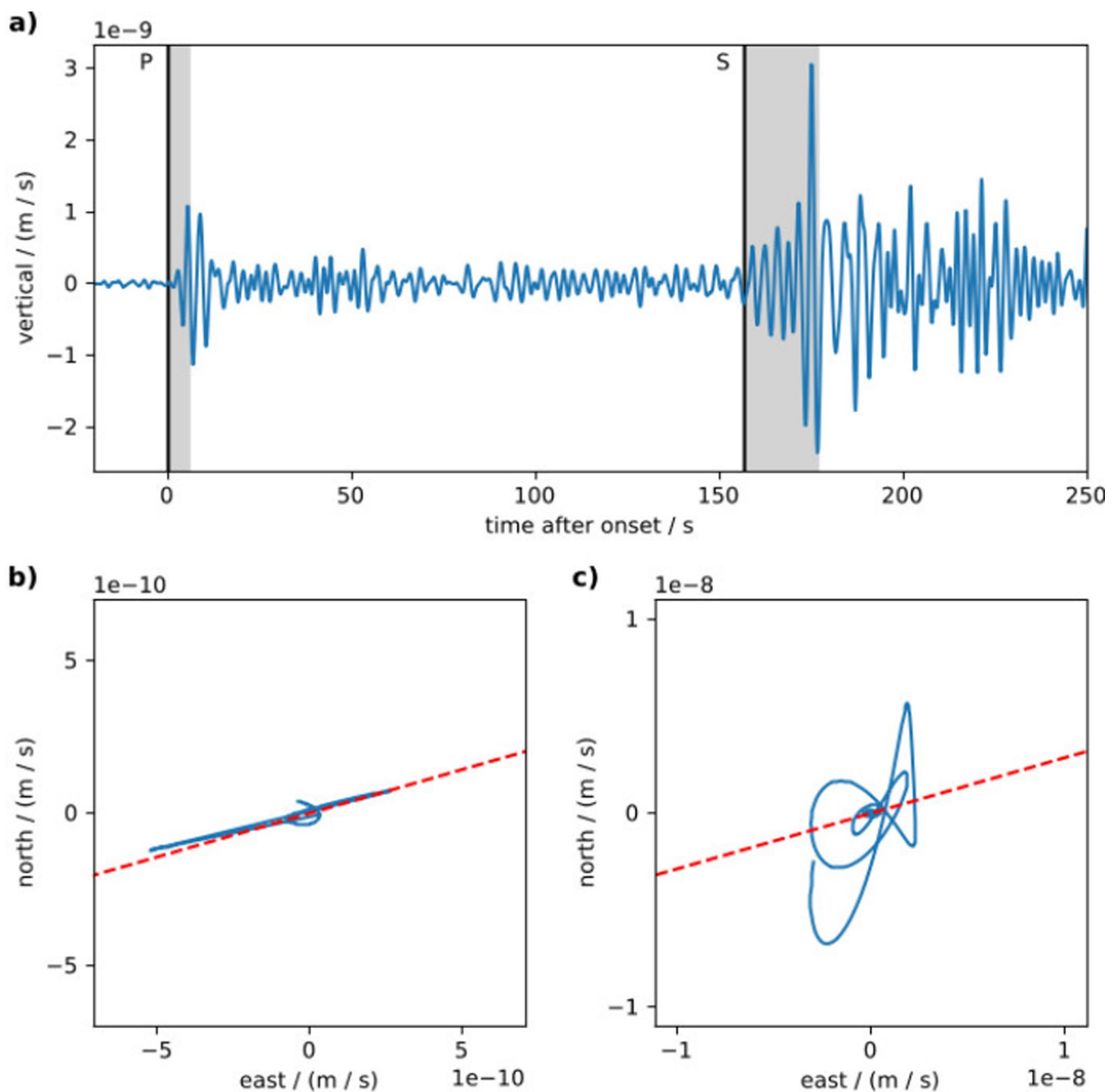
Extended Data Fig 3 | Event S0235a waveform and polarisation summary. a shows VBB vertical time series indicating the picks associated to P and S phases. **b** and **c** show horizontal hodograms for P and S windows respectively. The time windows used to produce the hodograms are indicated by the grey shaded regions on **a**. The event back azimuth is indicated in the red dotted line in **b** and **c**, matching the first P-wave motion. A 2-5s bandpass filter is applied.

Event name	Event quality	Aligned distance (°)	Catalogue distance (°)	Catalogue back-azimuth (°)	P pick (s) *Time (uncertainty)*	S pick (s) *Time (uncertainty)*	Magnitude M_W
Low Frequency events							
S0105a	B	27 (±5)	31 (±10)		2019-03-14 21:03:31 (±20)	2019-03-14 21:06:39 (±20)	3.2
S0133a	B	[90] (±20)	33 (±7)		2019-04-12 18:14:35 (±60)	2019-04-12 18:17:56 (±20)	3.2
S0154a	B	[90] (±20)	49 (±7)		2019-05-04 07:07:05 (±20)	2019-05-04 07:11:57 (±20)	3.5
S0167a	C	[150] (±20)					3.8
S0173a	A	28 (±3)	29 (±3)	91 (±5)	2019-05-23 02:22:59.1 (±1)	2019-05-23 02:25:53.8 (±2)	3.6
S0183a	C	47 (±10)		73 (±20)	2019-06-03 02:27:45.8 (±1)	2019-06-03 02:32:09 (±10)	3.1
S0185a	B	60 (±3)	59 (±10)		2019-06-05 02:13:51 (±20)	2019-06-05 02:19:35 (±20)	3.1
S0189a	B	27 (±5)	32 (±7)		2019-06-09 05:40:06 (±20)	2019-06-09 05:43:20 (±20)	3.0
S0205a	D	[45] (±10)					3.0
S0226b	C	[90] (±20)					
S0234c	D	65 (±5)					2.8
S0235b	A	25 (±3)	26 (±3)	74 (±15)	2019-07-26 12:19:19.3 (±2)	2019-07-26 12:21:56.1 (±2)	3.6
S0325a	B	35 (±5)	40 (±5)		2019-10-26 06:58:58.9 (±1)	2019-10-26 07:02:56 (±10)	3.7

					P_g pick (s)	S_g pick (s)	
High Frequency events							
S0128a	B		8		2019-04-07 09:33:36 (±20)	2019-04-07 09:35:00 (±20)	2.1
S0185b	B		31		2019-06-05 03:29:16 (±10)	2019-06-05 03:34:12 (±10)	2.0
S0202b	C		14		2019-06-22 14:01:35 (±20)	2019-06-22 14:04:08 (±20)	1.8
S0202c	C		24		2019-06-22 15:49:43 (±20)	2019-06-22 15:54:00 (±20)	1.9
S0218a	B		32		2019-07-09 05:03:01 (±20)	2019-07-09 05:08:37 (±20)	2.3
S0222a	B		20		2019-07-13 03:32:40 (±10)	2019-07-13 03:36:17 (±20)	1.6*
S0226a	C		9		2019-07-17 04:33:03 (±20)	2019-07-17 04:34:40 (±20)	1.5
S0228c	B		22		2019-07-19 09:38:29 (±10)	2019-07-19 09:42:21 (±20)	1.9
S0229a	B		26		2019-07-20 08:50:24 (±20)	2019-07-20 08:55:05 (±20)	1.6*
S0231b	B		24		2019-07-22 08:10:11 (±10)	2019-07-22 08:14:24 (±20)	1.9
S0234b	C		13		2019-07-25 12:35:15 (±20)	2019-07-25 12:37:37 (±20)	1.3*
S0239a	B		27		2019-07-30 14:17:03 (±10)	2019-07-30 14:21:49 (±10)	1.9
S0246a	B		26		2019-08-06 18:16:36 (±20)	2019-08-06 18:21:12 (±20)	1.8
S0257a	B		31		2019-08-18 00:23:06 (±20)	2019-08-18 00:28:34 (±20)	1.8*
S0257b	B		26		2019-08-18 01:05:46 (±10)	2019-08-18 01:10:26 (±20)	1.7*
S0260a	B		26		2019-08-21 05:11:21 (±10)	2019-08-21 05:15:55 (±20)	2.2
S0262b	C		25		2019-08-23 08:39:53 (±10)	2019-08-23 08:44:18 (±20)	2.2
S0263a	B		7		2019-08-23 11:09:54 (±10)	2019-08-23 11:11:04 (±10)	1.9
S0264e	B		35		2019-08-25 10:31:35 (±10)	2019-08-25 10:37:48 (±10)	2.2
S0289a	B		27		2019-09-20 00:02:04 (±20)	2019-09-20 00:06:49 (±20)	2.3
S0290a	C		22		2019-09-21 02:06:12 (±20)	2019-09-21 02:10:10 (±20)	1.6*
S0291c	B		23		2019-09-22 03:46:08 (±10)	2019-09-22 03:50:11 (±20)	2.0
S0292a	C		32		2019-09-23 03:46:08 (±20)	2019-09-23 03:51:48 (±20)	1.9

* M_W magnitudes are derived from the spectral magnitude (M_{FB}^{Ma}), except for those indicated with * which are based on the 2.4Hz magnitude ($M_{2.4Hz}^{Ma}$)

Extended Data Fig 4 | List of events analysed in this paper. Event quality is as defined in the Methods section. The aligned distances follow Fig. 3, while the distance, back azimuth and phase picks from the MQS catalogue are provided when available. The moment magnitude (M_W) is based on the spectral magnitude except for those events marked with an asterisk, that are derived from the 2.4Hz magnitude (Supplementary Information SI3).

Event name	f_{min}	f_{max}	SNRs from spectral envelopes				Signal start	Signal end
			Peak signal/ peak noise	Mean signal/ mean noise	max(P)/max(noise)	max(S)/max(noise)		
Low frequency								
S0105a	0.31	0.5	7.8	6.1	4.7	7.8	2019-03-14 20:53:28	2019-03-14 21:28:57
S0133a	0.33	0.67	10.5	6.5	6.3	10.5	2019-04-12 18:04:34	2019-04-12 18:38:48
S0154a	0.17	0.67	7.7	6.8	6.9	7.7	2019-05-04 6:57:00	2019-05-04 7:37:48
S0167a	0.18	0.47	4.9	2.8	3.6	4.9	2019-05-17 16:37:15	2019-05-17 17:13:27
S0173a	0.18	0.67	95	16.9	19	95	2019-05-23 2:12:48	2019-05-23 3:10:23
S0183a	0.3	0.8	5.3	2.8	5.3	1.7	2019-06-03 2:17:47	2019-06-03 3:01:07
S0185a	0.29	0.83	14.1	5.4	5.2	14.1	2019-06-05 2:03:25	2019-06-05 2:49:55
S0189a	0.36	0.83	10.6	5.1	5	10.6	2019-06-09 5:30:05	2019-06-09 6:07:57
S0205a	0.3	0.8	4.8	3.8	4.8		2019-06-25 16:59:43	2019-06-25 17:43:03
S0226b	0.33	0.83	5.1	2.5	2.3	5.1	2019-07-17 5:33:38	2019-07-17 6:12:49
S0234c	0.33	0.83	3.8	2.4	2.4	3.8	2019-07-25 12:44:18	2019-07-25 13:19:32
S0235b	0.2	0.85	251.7	25.2	31	251.7	2019-07-26 12:09:16	2019-07-26 13:28:08
S0325a	0.3	0.8	3.5	2.9	3.5	3.2	2019-10-26 6:48:58	2019-10-26 7:28:35
High-frequency								
S0128a	2	3	7.2	3.2	1	7.2	2019-04-07 9:23:36	2019-04-07 10:06:56
S0185b	2	3	10.8	3.9	3.7	10.8	2019-06-05 3:19:15	2019-06-05 3:55:25
S0202b	2	3	3	1.6	1.2	3	2019-06-22 13:51:40	2019-06-22 14:35:00
S0202c	2	3	5.5	2.9	2.3	5.5	2019-06-22 15:40:25	2019-06-22 16:17:28
S0218a	2	3	11.6	5.1	5.3	11.6	2019-07-09 4:53:00	2019-07-09 5:28:53
S0222a	2	3	3.5	2.4	1.4	3.5	2019-07-13 3:22:44	2019-07-13 4:06:04
S0226a	2	3	3.1	2.2	1.2	3.1	2019-07-17 4:23:02	2019-07-17 5:06:22
S0228c	2	3	7.5	3.6	3	7.5	2019-07-19 9:28:15	2019-07-19 10:02:21
S0229a	2	3	3.9	2.2	3.1	3.9	2019-07-20 8:40:08	2019-07-20 9:14:03
S0231b	2	3	6.9	4.8	2.8	6.9	2019-07-22 7:59:53	2019-07-22 8:33:42
S0234b	2	3	1.5	1.2	1.3	1.5	2019-07-25 12:25:08	2019-07-25 13:08:28
S0239a	2	3	11.5	5	7.2	11.5	2019-07-30 14:06:49	2019-07-30 14:42:10
S0246a	2	3	7.4	4.1	2.5	7.4	2019-08-06 18:05:50	2019-08-06 18:42:02
S0257a	2	3	5	3.2	4.7	5	2019-08-18 0:13:04	2019-08-18 0:46:46
S0257b	2	3	6.8	4.6	2.8	6.8	2019-08-18 0:55:34	2019-08-18 1:38:54
S0260a	2	3	38.3	15.6	17	38.3	2019-08-21 5:01:08	2019-08-21 5:38:41
S0262b	2	3	5.5	2.5	1.2	5.5	2019-08-23 8:29:46	2019-08-23 9:00:34
S0263a	2	3	17.4	13.2	1.4	17.4	2019-08-23 10:59:44	2019-08-23 11:43:04
S0264e	2	3	47.9	21	44.8	47.9	2019-08-25 10:21:36	2019-08-25 11:04:18
S0289a	2	3	18.1	9.9	6.7	18.1	2019-09-19 23:51:50	2019-09-20 0:27:52
S0290a	2	3	3.5	1.8	1.7	3.5	2019-09-21 1:56:14	2019-09-21 2:30:56
S0291c	2	3	11.1	5.9	3.8	11.1	2019-09-22 3:36:12	2019-09-22 4:10:24
S0292a	2	3	8	4.3	4.3	8	2019-09-23 3:34:42	2019-09-23 4:11:48

Extended Data Fig 5 | SNR values for the events analysed in this paper. Frequency range used for computing the spectral envelopes are listed in the second and third columns. Four different SNR types computed using maxima and means of signal and noise, as well as maxima of P- and S envelopes are also given with the start and end times of the signal used. Events with little or no S-wave energy are also evident from the relative amplitude of SNRs (shaded cells).
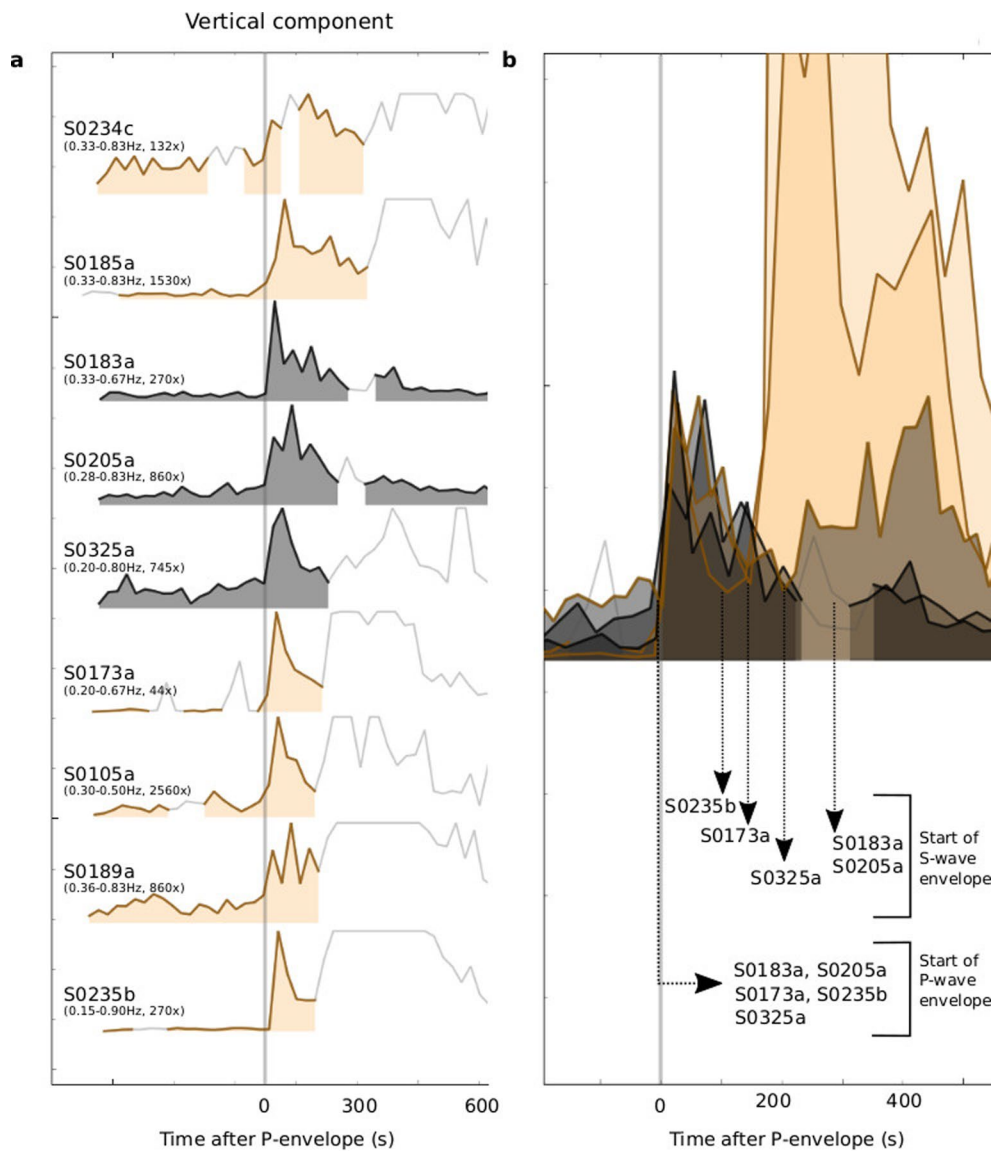
Extended Data Fig 6 | Alignment of events with P-wave arrivals using vertical spectral envelopes. a, All events with P-wave energy aligned on a reference line; events are equally spaced sorted by distance; for each event we indicate the frequency band used to derive the spectral envelope and the amplification used in the display, so that all P waves have the same amplitude; glitches and the following S-wave are blanked out. **b**, P-wave envelopes overlapped for four of the events in the left panel; envelope amplitudes are re-scaled to show the similarity; S0173a and S0235b have clear P- and S-wave arrivals, while we observe only a strong first phase for S0183a and S0205a, interpreted as P-phase, and a weak second phase, interpreted as S-phase. The colour code of the events is the same used in Fig. 3. The spectral window length in **b** is 40 s to increase the visibility of the S-wave onsets.
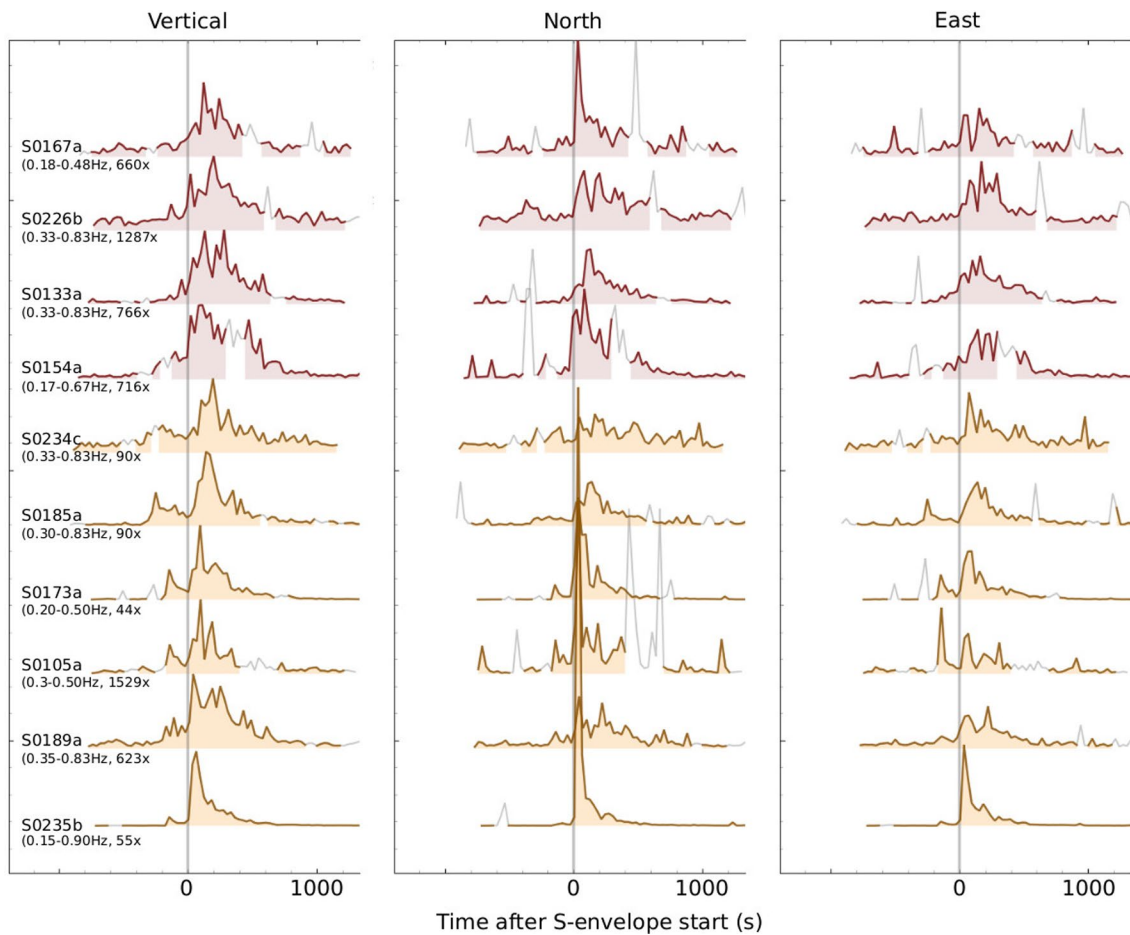
Extended Data Fig 7 | Alignment of events using their S-wave envelopes along a reference line. The top four events have significantly longer S-wave envelopes. S0183a and S0205a are not included as these events do not display a clearly visible S-wave. The colour code of the events is the same used in Fig. 3.